TECHNISCHE MECHANIK, 32, 2-5, (2012), 369 – 379
submitted: October 10, 2011

Computational Homogenisation of Polycrystalline Elastoplastic Microstructures at Finite Deformation

E. Lehmann, S. Loehnert, P. Wriggers

During sheet bulk metal forming processes, both flat geometries and three-dimensional structures change their shape while undergoing large plastic deformations. As for metal forming processes, FE-simulations are often done before in-situ experiments, a very accurate model for respective structures is required, performing well at small geometries possessing small curvatures as forms with wide as well as lateral characteristics.
Because of the crystalline nature of metals, certain anisotropies have to be taken into account. Macroscopically observable plastic deformation is traced back to dislocations within considered slip systems in the crystals causing plastic anisotropy on the microscopic and the macroscopic level.
A crystal plasticity model for finite deformations is used to model the behaviour of polycrystalline materials in representative volume elements (RVEs) on the microstructure. In order to circumvent singularities stemming from the linear dependency of the slip system vectors, a viscoplastic power-law is introduced providing the evolution of the plastic slips and slip resistances. The model is validated with experimental microstructural data under deformation. Through homogenisation and optimisation techniques, effective stress-strain curves are determined and can be compared to results from real forming processes, leading to an effective elastoplastic material model which is suitable for processes in the sheet bulk metal forming field.

1 Introduction

Phenomenological macroscopic observations of metals do not acknowledge actual heterogeneities in the microstructure at once. For some time, the mechanics of heterogeneous and polycrystalline materials have been limited to the formulation of simplified models taking into account some aspects of the microstructural characteristics. However, the proceeding increase of computational capabilites enables a more elaborated approach towards the development of a suitable material model for specific requirements and numerical simulations in the forming field. At the same time, modelling the microstructure is already a complex task as certain microstructural properties have to be considered. On the microscopic level of metals, anisotropies have to be taken into account stemming from dislocations occurring on the atomic lattice within considered slip systems. Such mechanisms are macroscopically observed as plastic anisotropic yielding.

In order to take into account the microstructural complexity on the one hand and aiming at the ability to compute real manufacturing and forming processes on the other hand, a macroscopic effective material model which sufficiently represents the microstructure has to be developed. Due to the various different boundary conditions the material can be constrained to during fabrication stages, it has to be validated for these applications. A huge challenge appears in the attempt to fulfil the requirements of both sheet and bulk metal forming processes. In doing so, the model approach has naturally to be performed in a three-dimensional way, although the structure can certainly be constrained to any geometrical limit or constitution. A validation and comparison to real microstructures is performed with two-dimensional specimen and distributed data within this contribution. However, the dislocation movement on the microstructure evolves in three required directions.

2 Constitutive Framework: Finite Multiplicative Multisurface Elastoplasticity

The deformation gradient $\boldsymbol{F} = {}^{\partial \boldsymbol{x}}/_{\partial \boldsymbol{X}}$ with Jacobian $\mathrm{J} = \det \boldsymbol{F} > 0$ maps tangent vectors of material lines in the reference configuration $\mathcal{B} \in \mathbb{R}^3$ onto tangent vectors of deformed lines in the current configuration $\mathcal{B}_\mathrm{t} \in \mathbb{R}^3$ and is decomposed into an elastic and a plastic part. The elastic part $\boldsymbol{F}^e$ contributes to stretching and rigid body rotation

of the crystal lattice, the plastic part $\boldsymbol{F}^p$ characterises plastic flow caused by dislocations on defined slip systems

$$\boldsymbol{F} = \boldsymbol{F}^e \boldsymbol{F}^p. \tag{1}$$

The multiplicative split assumes a local unstressed intermediate configuration defined by the plastic deformation gradient, see Fig. 1, which can be determined through an evolution assumption and whose initial condition is assumed to be $\boldsymbol{F}_0^p = \mathbf{1}$.

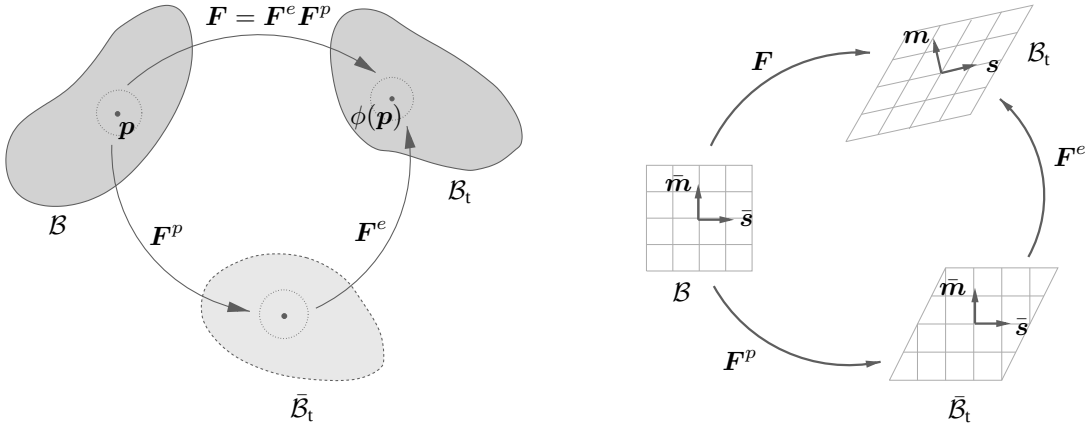

(a) Continuum mechanical framework (b) Crystallographic conception

Figure 1: Multiplicative elasto-plastic decomposition of the deformation gradient $\boldsymbol{F}$

Further, a volumetric-deviatoric split of the deformation gradient and its constituents is performed

$$\boldsymbol{F}_\mathrm{iso} = \mathrm{J}^{-1/3}\boldsymbol{F}, \quad \boldsymbol{F}^e_\mathrm{iso} = \mathrm{J}^{e\,-1/3}\boldsymbol{F}^e, \quad \boldsymbol{F}^p_\mathrm{iso} = \mathrm{J}^{p\,-1/3}\boldsymbol{F}^p, \tag{2}$$

with $\mathrm{J} = \mathrm{J}^e$ due to fulfilling the requirement of present plastic incompressibility expressed through $\mathrm{J}^p = 1$.

2.1 Thermodynamical Considerations

The deformation power per unit undeformed volume can be written as

$$\boldsymbol{P} : \dot{\boldsymbol{F}} = \bar{\boldsymbol{P}} : \dot{\boldsymbol{F}}^e + \bar{\boldsymbol{\Sigma}} : \bar{\boldsymbol{L}}^p, \tag{3}$$

where $\bar{\boldsymbol{P}} = \boldsymbol{P}\boldsymbol{F}^{p\,T}$ is the 1st PIOLA-KIRCHHOFF stress tensor relative to the intermediate configuration $\bar{\mathcal{B}}_\mathrm{t}$ and $\bar{\boldsymbol{\Sigma}} = \boldsymbol{F}^{e\,T}\boldsymbol{P}\boldsymbol{F}^{p\,T} = \boldsymbol{F}^{e\,T}\boldsymbol{\tau}\boldsymbol{F}^{e\,-T}$ a stress measure conjugate to the plastic velocity gradient $\bar{\boldsymbol{L}}^p = \dot{\boldsymbol{F}}^p\boldsymbol{F}^{p\,-1}$ on $\bar{\mathcal{B}}_\mathrm{t}$, $\boldsymbol{\tau}$ being the KIRCHHOFF stress tensor on $\mathcal{B}_\mathrm{t}$. Further, it is

$$\bar{\boldsymbol{P}} = \boldsymbol{F}^e\bar{\boldsymbol{S}}, \quad \bar{\boldsymbol{S}} = \bar{\boldsymbol{C}}^{e\,-1}\bar{\boldsymbol{\Sigma}}, \quad \bar{\boldsymbol{C}}^e = \boldsymbol{F}^{e\,T}\boldsymbol{F}^e, \tag{4}$$

where $\bar{\boldsymbol{S}}$ is the 2nd PIOLA-KIRCHHOFF stress tensor relative to the intermediate configuration $\bar{\mathcal{B}}_\mathrm{t}$ which is symmetric, $\bar{\boldsymbol{C}}^e$ is further the elastic right CAUCHY-GREEN tensor on $\bar{\mathcal{B}}_\mathrm{t}$.

The evolution of the plastic deformation gradient $\boldsymbol{F}^p$ is defined by the plastic flow equation, resulting from the plastic rate of deformation $\bar{\boldsymbol{L}}^p$. In the presence of n_syst systems undergoing plastic slip, represented by the plastic shear rates $\dot{\gamma}^\alpha$, the plastic flow equation is further generalised

$$\bar{\boldsymbol{L}}^p = \dot{\boldsymbol{F}}^p\boldsymbol{F}^{p\,-1}, \quad \bar{\boldsymbol{L}}^p = \sum_{\alpha=1}^{n_\mathrm{syst}} \dot{\gamma}^\alpha \bar{\boldsymbol{s}}^\alpha \otimes \bar{\boldsymbol{m}}^\alpha, \tag{5}$$

$\bar{\boldsymbol{s}}^\alpha$ being the slip direction vector and $\bar{\boldsymbol{m}}^\alpha$ being the slip plane normal vector of the α-th slip system $\{\bar{\boldsymbol{s}}^\alpha, \bar{\boldsymbol{m}}^\alpha\}$. The slip system vectors have the properties $\bar{\boldsymbol{s}} \cdot \bar{\boldsymbol{m}} = 0$ and thus $(\bar{\boldsymbol{s}}^\alpha \otimes \bar{\boldsymbol{m}}^\alpha)(\bar{\boldsymbol{s}}^\alpha \otimes \bar{\boldsymbol{m}}^\alpha) = \mathbf{0}$. The generalisation

in (5) leads to the modified evolution equation of the plastic deformation gradient depending on the plastic slips

$$\dot{\boldsymbol{F}}^p = \left[\sum_\alpha \dot{\gamma}^\alpha \, \bar{\boldsymbol{s}}^\alpha \otimes \bar{\boldsymbol{m}}^\alpha \right] \boldsymbol{F}^p. \tag{6}$$

2.2 The Resolved SCHMID Stress

The SCHMID stress τ^α is the projection of $\bar{\boldsymbol{\Sigma}}$ onto the slip system $\bar{\boldsymbol{s}}^\alpha \otimes \bar{\boldsymbol{m}}^\alpha$

$$\tau^\alpha = (\mathrm{dev}[\bar{\boldsymbol{\Sigma}}] \cdot \bar{\boldsymbol{m}}^\alpha) \cdot \bar{\boldsymbol{s}}^\alpha = \mathrm{dev}[\bar{\boldsymbol{\Sigma}}] : \bar{\boldsymbol{s}}^\alpha \otimes \bar{\boldsymbol{m}}^\alpha. \tag{7}$$

As the slip system tensor $\bar{\boldsymbol{s}}^\alpha \otimes \bar{\boldsymbol{m}}^\alpha$ is purely deviatoric, only the deviator of the stress tensor contributes to the resolved stress. With the relations in (4) and some straightforward recast, it is

$$\tau^\alpha = \boldsymbol{R}^{e\,T} \boldsymbol{\tau} \boldsymbol{R}^e : \bar{\boldsymbol{s}}^\alpha \otimes \bar{\boldsymbol{m}}^\alpha. \tag{8}$$

2.3 Elastic Response

The elastic part of the deformation is gained from a NEO-HOOKEean strain energy function. It is assumed that large plastic strains occur during metal forming processes and dominate the forming behaviour and the elastic strains remain small relative to the plastic strains. Thus, the choice of the appearance of the elastic response is rather arbitrary and can be assumed to be isotropic. The description is hence given in terms of the elastic left CAUCHY-GREEN tensor $\boldsymbol{b}^e$. Applying a volumetric-deviatoric split yields

$$\rho\psi(\boldsymbol{b}^e_{\text{iso}}, \mathrm{J}^e) = \frac{\mu}{2} \left(\mathrm{tr}\, \boldsymbol{b}^e_{\text{iso}} - 3 \right) + \frac{\kappa}{2} \left(\ln \mathrm{J}^e \right)^2 \tag{9}$$

$$\boldsymbol{\tau} = 2\,\rho\, \frac{\partial \psi}{\partial \boldsymbol{b}^e}\, \boldsymbol{b}^e = \mu\, \mathrm{dev}(\boldsymbol{b}^e_{\text{iso}}) + \kappa\, \ln \mathrm{J}^e\, \boldsymbol{1}, \quad \mathrm{dev}(\boldsymbol{\tau}) = \mu\, \mathrm{dev}(\boldsymbol{b}^e_{\text{iso}}),\ \mathrm{vol}(\boldsymbol{\tau}) = \kappa\, \ln \mathrm{J}^e\, \boldsymbol{1}. \tag{10}$$

Because slip-system tensors are deviatoric by construction, their internal product by the hydrostatic KIRCHHOFF stress components vanishes and the SCHMID stress in (8) remains

$$\tau^\alpha = \mu\, \bar{\boldsymbol{s}}^\alpha_{\text{iso}} \cdot \bar{\boldsymbol{m}}^\alpha_{\text{iso}}, \quad \bar{\boldsymbol{s}}^\alpha_{\text{iso}} = \boldsymbol{F}^e_{\text{iso}} \cdot \bar{\boldsymbol{s}}^\alpha, \quad \bar{\boldsymbol{m}}^\alpha_{\text{iso}} = \boldsymbol{F}^e_{\text{iso}} \cdot \bar{\boldsymbol{m}}^\alpha. \tag{11}$$

2.4 A Rate-Dependent Formulation via a Viscoplastic Power-Law

A rate-dependent theory enables the modeling of creep in single crystals and is performed by the introduction of a power law-type constitutive equation for the rates $\dot{\gamma}^\alpha$ of inelastic deformation in the slip systems

$$\dot{\gamma}^\alpha = \dot{\gamma}_0\, \frac{\tau^\alpha}{\tau_y} \left(\frac{|\tau^\alpha|}{\tau_y} \right)^{m-1} = \dot{\gamma}_0\, \tau^\alpha\, |\tau^\alpha|^{m-1}\, \tau_y^{-m}, \tag{12}$$

$\dot{\gamma}_0$ and τ_y being the reference shear rate and slip resistance, and m being a rate-sensivity parameter. Within an isotropic TAYLOR hardening model, the evolution for the slip resistance τ_y is considered

$$\dot{\tau}_y = \sum_\alpha H \cdot |\dot{\gamma}^\alpha|, \quad \gamma = \int_0^t \dot{\gamma}\, dt, \quad \dot{\gamma} = \sum_\alpha \dot{\gamma}^\alpha. \tag{13}$$

3 Incremental Kinematics

The slip rate is discretised with a standard backward EULER integration in order to obtain incremental evolution equations for the update of the evolving quantities

$$\Delta\gamma^\alpha = \Delta t\, \dot{\gamma}^\alpha \left(\boldsymbol{F}^e \right). \tag{14}$$

The implicit exponential integrator is then used to discretise the plastic flow equation (6)

$$\boldsymbol{F}^p_{n+1} = \exp\left[\sum_\alpha \Delta\gamma^\alpha \bar{\boldsymbol{s}}^\alpha \otimes \bar{\boldsymbol{m}}^\alpha\right] \cdot \boldsymbol{F}^p_n. \tag{15}$$

Due to the property $\det[\exp(\bar{\boldsymbol{s}}^\alpha \otimes \bar{\boldsymbol{m}}^\alpha)] = \exp[\mathrm{tr}\,(\bar{\boldsymbol{s}}^\alpha \otimes \bar{\boldsymbol{m}}^\alpha)] = \exp(0) = 1$, it preserves the plastic volume. Here, $\boldsymbol{F}^{e\,\mathrm{trial}}_{n+1} = \boldsymbol{f}_{n+1}\,\boldsymbol{F}^e_n$, is the *trial* elastic deformation gradient with $\boldsymbol{f}_{n+1} = \boldsymbol{F}_{n+1}\,\boldsymbol{F}^{-1}_n = \boldsymbol{1} + \mathrm{grad}_n\,(\Delta\boldsymbol{u})$ and $\mathrm{J}_{n+1} = \det \boldsymbol{F}_{n+1}$, $\boldsymbol{F}^{e\,\mathrm{trial}}_{\mathrm{iso}} = \mathrm{J}^{-1/3}_{n+1}\,\boldsymbol{F}^{e\,\mathrm{trial}}_{n+1}$, so that an exponential update for the new elastic deformation gradient can be obtained

$$\boldsymbol{F}^e_{n+1} = \boldsymbol{F}^{e\,\mathrm{trial}}_{n+1} \cdot \exp\left[\sum_\alpha -\Delta\gamma^\alpha \bar{\boldsymbol{s}}^\alpha \otimes \bar{\boldsymbol{m}}^\alpha\right]. \tag{16}$$

The current *trial* resolved shear stress $\tau^{\alpha\,\mathrm{trial}}_{n+1}$, cf. (11), is obtained with the current orientation of the crystal through rotation of the slip system with the trial elastic deformation gradient

$$\tau^{\alpha\,\mathrm{trial}}_{n+1} = \mu\,\bar{\boldsymbol{s}}^{\alpha\,\mathrm{trial}}_{\mathrm{iso}} \cdot \bar{\boldsymbol{m}}^{\alpha\,\mathrm{trial}}_{\mathrm{iso}}, \quad \bar{\boldsymbol{s}}^{\alpha\,\mathrm{trial}}_{\mathrm{iso}} = \boldsymbol{F}^{e\,\mathrm{trial}}_{\mathrm{iso}} \cdot \bar{\boldsymbol{s}}^\alpha, \quad \bar{\boldsymbol{m}}^{\alpha\,\mathrm{trial}}_{\mathrm{iso}} = \boldsymbol{F}^{e\,\mathrm{trial}}_{\mathrm{iso}} \cdot \bar{\boldsymbol{m}}^\alpha. \tag{17}$$

3.1 Equilibrating the Plastic State

Omitting the subscript $n+1$, a residual based on the exponential map is defined to equilibrate the plastic state, leading to a local NEWTON-RAPHSON algorithm through a TAYLOR expansion about the reached point $\boldsymbol{F}^e_k$

$$\boldsymbol{R}(\boldsymbol{F}^e) := \boldsymbol{F}^e - \boldsymbol{F}^{e\,\mathrm{trial}} \cdot \exp\left[\sum_\alpha -\Delta\gamma^\alpha \bar{\boldsymbol{s}}^\alpha \otimes \bar{\boldsymbol{m}}^\alpha\right] = \boldsymbol{0}, \tag{18}$$

and

$$\boldsymbol{R}_k + \partial_{\boldsymbol{F}^e_k} \boldsymbol{R}(\boldsymbol{F}^e_k) : \Delta\boldsymbol{F}^e_k = \boldsymbol{0}, \tag{19}$$

$$\Delta\boldsymbol{F}^e_k = -\left[\partial_{\boldsymbol{F}^e_k} \boldsymbol{R}(\boldsymbol{F}^e_k)\right]^{-1} : \boldsymbol{R}_k, \quad \boldsymbol{F}^e_{k+1} = \boldsymbol{F}^e_k + \Delta\boldsymbol{F}^e_k, \tag{20}$$

with the important derivatives

$$[\partial_{\boldsymbol{F}^e} \boldsymbol{R}(\boldsymbol{F}^e)]_{ijkl} = \delta_{ik}\delta_{jl} + F^{e\,\mathrm{trial}}_{im}\,\mathbb{E}_{mjpq}\left[\sum_\alpha \bar{\boldsymbol{s}}^\alpha \otimes \bar{\boldsymbol{m}}^\alpha \otimes \partial_{\boldsymbol{F}^e}\,\Delta\gamma^\alpha\right]_{pqkl} \tag{21}$$

$$\mathbb{E}_{mjpq} = \frac{\partial \exp\left(\left[-\sum_\alpha \Delta\gamma^\alpha(\boldsymbol{F}^e)\,\bar{\boldsymbol{s}}^\alpha \otimes \bar{\boldsymbol{m}}^\alpha\right]_{mj}\right)}{\partial\left[-\sum_\alpha \Delta\gamma^\alpha(\boldsymbol{F}^e)\,\bar{\boldsymbol{s}}^\alpha \otimes \bar{\boldsymbol{m}}^\alpha\right]_{pq}}, \tag{22}$$

and

$$\partial_{\boldsymbol{F}^e}\,\Delta\gamma^\beta = \Delta t\,\dot\gamma_0\,m\,|\tau^\alpha|^{m-1}\,\tau_y^{-m}\left[\Xi^{\alpha\,\beta}\right]^{-1}\,\partial_{\boldsymbol{F}^e}\,\tau^\alpha \tag{23}$$

$$\partial_{\boldsymbol{F}^e}\,\tau^\alpha = -\frac{2}{3}\,\tau^\alpha\,\boldsymbol{F}^{e\,-T} + \mu\,\mathrm{J}^{-1/3}\,[\bar{\boldsymbol{m}}^\alpha_{\mathrm{iso}} \otimes \bar{\boldsymbol{s}}^\alpha + \bar{\boldsymbol{s}}^\alpha_{\mathrm{iso}} \otimes \bar{\boldsymbol{m}}^\alpha] \tag{24}$$

$$\Xi^{\alpha\,\beta} = \delta^{\alpha\,\beta} + \Delta t\,\dot\gamma_0\,m\,\tau^\alpha\,|\tau^\alpha|^{m-1}\,\tau_y^{-m-1}\sum\nolimits_\beta H\,\mathrm{sign}(\Delta\gamma^\beta). \tag{25}$$

4 Polycrystalline Model

4.1 VORONOI Cell Grains

The polycrystal is modelled with three-dimensional VORONOI cell shaped grains. Through the DELAUNAY triangulation of a given random point seed, a polycrystal of arbitrary size can be obtained. The crystal grains are embedded in a bounding box of stated size (Fig. 2(a)) and meshed with tetrahedral finite elements based on a reasonable edge size ratio.

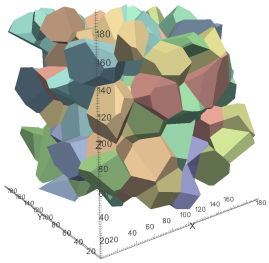

(a) Polycrystal consisting of VORONOI cell grains.

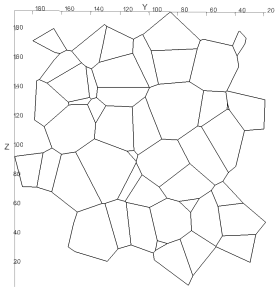

(b) Cut through polcrystalline structure.

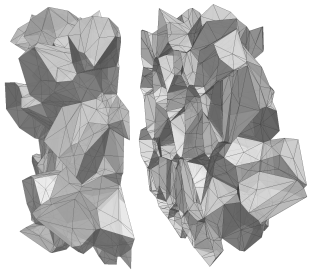

(c) Three-dimensional view into the cutted polycrystal.

Figure 2: Polycrystalline model within bounding box $200 \times 200 \times 200$ μm. The VORONOI cell shaped crystal grains are obtained through DELAUNAY triangulation of a random point seed.

4.2 Microstructural Effects

In order to understand the microstructural model, the modelled microstructural effects have to be analysed. Nevertheless, the microstructural validation is performed in order to be able to determine and capture particular macroscopic effects. The development of an overall macroscopic material model remains in focus. For the validation of the model, a real structure which is analysed under a scanning electron microscope (SEM) is taken into consideration. Experimentally obtained data is included in the simulation input, e.g. EULER angles and the grain size distribution of the polycrystalline structure at hand. Whereas the orientations, e.g. the EULER angles and the SCHMID factors, of the real structure in the SEM is taken pixelwise from a two-dimensional view onto the polycrystal, those of the simulations are evaluated elementwise for a three-dimensional specimen. For differently orientated grains, all slip systems are reorientated according to the BUNGE convention with the three angles ϕ_1, Φ and ϕ_2

$$\boldsymbol{R}_{\Psi} = \begin{bmatrix} 1 & 0 & 0 \\ & \cos\phi_1 & -\sin\phi_1 \\ 0 & \sin\phi_1 & \cos\phi_1 \end{bmatrix} \quad \boldsymbol{R}_{\Theta} = \begin{bmatrix} \cos\Phi & -\sin\Phi & 0 \\ \sin\Phi & \cos\Phi & 0 \\ 0 & 0 & 1 \end{bmatrix} \quad \boldsymbol{R}_{\Phi} = \begin{bmatrix} 1 & 0 & 0 \\ & \cos\phi_2 & -\sin\phi_2 \\ 0 & \sin\phi_2 & \cos\phi_2 \end{bmatrix}, \tag{26}$$

$$\boldsymbol{R} = \boldsymbol{R}_{\phi_1} \cdot \boldsymbol{R}_{\Phi} \cdot \boldsymbol{R}_{\phi_2}. \tag{27}$$

For the finite element simulations, the bulk modulus is $\kappa = 152.2$ GPa and the shear modulus $\mu = 79.3$ GPa. The plastic parameters are the initial critical shear stress $\tau_{y\,0} = 80$ MPa, the reference shear stress $\dot{\gamma}_0 = 0.001\,/s$, the hardening modulus $H = 150$ MPa and the rate sensivity parameter $m = 5.0$. The bcc slip system vectors are chosen according to Tab. 1 for pre-texturing the material as in the experiment. The significant effect lies in the rotation of the slip systems with EULER angles so that the crystalline structure is represented for a considered ferritic steel (DC 04). The lattice constitution is thus present.

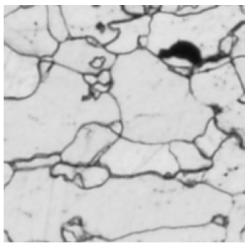

(a) Undeformed structure.

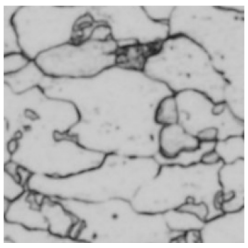

(b) 10 % deformed structure.

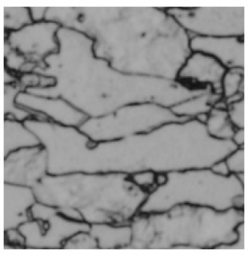

(c) 20 % deformed structure.

Figure 3: Deformed polycrystalline microstructure from SEM data. *Source: Institute of Materials Science, Leibniz Universität Hannover, Germany.*

In Fig. 3 a polycrystalline microstructure from the SEM is shown. In contrast, Fig. 4 shows the simulation of the microstructure under uniaxial tension incorporating EULER angles and grain size distribution of the real structure. The stretching of the grains in the tension direction can be covered, and also the necking of the specimen is modelled.

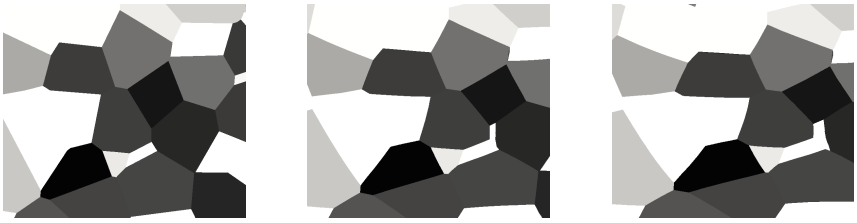

(a) Undeformed structure. (b) 10 % deformed structure. (c) 20 % deformed structure.

Figure 4: Deformed polycrystalline microstructure from finite element simulation.

Moreover, the SCHMID factor and the SCHMID stress are in focus of the analysis. For a uniaxial test, the definition of the SCHMID factor is given through Fig. 5(a); a dislocation is moving due to a force acting in the direction of the slip. Hence, the resulting shear stress in the slip system is significant for the dislocation movement, expressed in terms of the SCHMID stress τ^α, see (11), or also the SCHMID factor S^α of the α-th slip system. The SCHMID factor S^α is expressed through the angle θ between slip direction $\bar{\boldsymbol{s}}^\alpha$ and force F and the angle β between slip normal $\bar{\boldsymbol{m}}^\alpha$ and force F. As the increase of the SCHMID factor S^α refers to a more favourable orientation of the slip system with respect to plastic deformation, the maximal SCHMID factor is defined as

$$S^\alpha = \cos\theta \cdot \cos\beta \tag{28}$$

$$S := \max(S^\alpha) \qquad \text{for slip system } \alpha = 1, \ldots, n_{\text{syst}}. \tag{29}$$

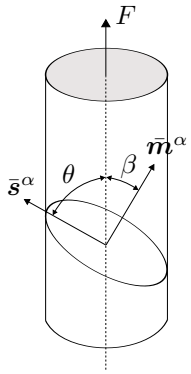

(a) Definition of the SCHMID factor: angle relations between stress state and slip system normal $\bar{\boldsymbol{m}}^\alpha$ and direction $\bar{\boldsymbol{s}}^\alpha$ in the single slip case for uniaxial tension.

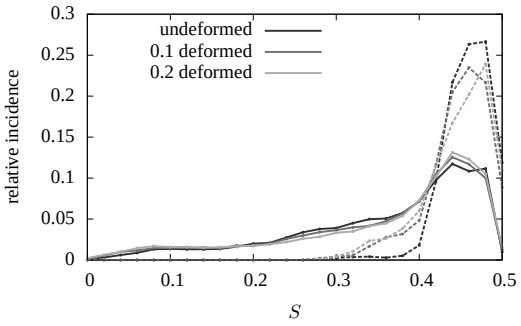

(b) Relative incidence of the maximal SCHMID factor in a polycrystalline structure of 308 crystal grains in uniaxial tension. Lines refer to simulation, dashed lines to experimental results.

Figure 5: The SCHMID factor. Definition and relative incidence in a polycrystalline structure.

In Fig. 5(b), the relative incidence of the maximal SCHMID factor S is given for the experimentally analysed and the simulated polycrystalline structure at hand. The increase of colour brightness corresponds to the increase of deformation, whereas simulated values are shown with lines and the experimentally obtained data with dashed lines. The simulation varifies the large amount of high SCHMID factors from the experiment, whereas the simulation results show more smaller factors. The height of the curves from simulation and experiment varies significantly, however, this can be traced back to the fact that the experimental results refer to a two-dimensional, pixelwise extract from the SEM and the simulation results to a three-dimensional, elementwise evaluation of the model. The qualitative behaviour of simulation and experiment yet matches.

The SCHMID stress τ^α is a resolved shear stress on the slip system accounting for the activation of slip. Fig. 6 illustrates the occurring maximal SCHMID stress over all the finite elements throughout the polycrystalline structure. A smaller polycrystal of only 6 crystal grains is shown in Fig. 6(a), where the good resolution within the slip plane can be observed. The 6 grains can be spotted through the varying orientation of slip systems in the grain, for larger polycrystalline structures (Fig. 6(b)) the resolved stress response gets blurer due to the grain increase, however, the same effect applies.

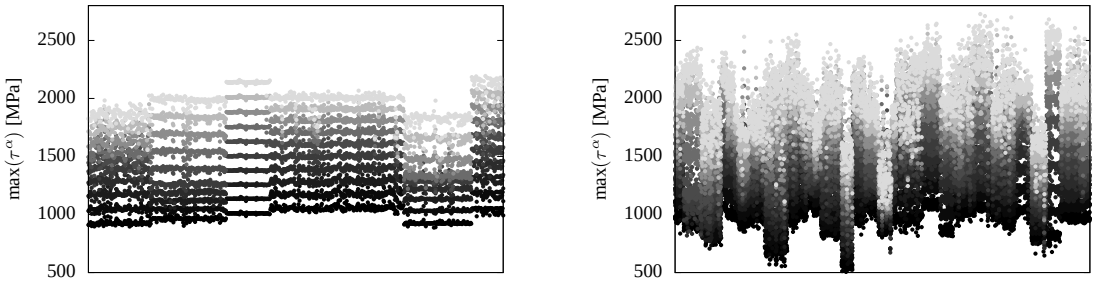

(a) Polycrystalline structure with 6 crystal grains.

(b) Polycrystalline structure with 32 crystal grains.

Figure 6: Maximal SCHMID stresses over all finite elements in the simulated polycrystalline structure.

5 Numerical Homogenisation

The calculation of the real structural component on the microscale fails due to inclusions, defects, crystallographic slip and localisation effects on the large discretisation effort and the computational expense. Based on the microstructure, effective and position-independent material parameters are to be determined within a homogenisation procedure, being representative for the heterogeneous structure in terms of a representative volume element (RVE).

5.1 Volume Average

In order to approach the prediction of an overall material behaviour of the representative volume element and hence of the macroscopic material, the volume averages of the deformation gradient $\boldsymbol{F}$ and the 1st PIOLA-KIRCHHOFF stress tensor $\boldsymbol{P}$ over the volume $V = \int_\Omega \mathrm{d}\Omega$ are defined as

$$\langle \boldsymbol{F} \rangle_\Omega := \frac{1}{V} \int_\Omega \boldsymbol{F} \ \mathrm{d}\Omega \tag{30}$$

$$\langle \boldsymbol{P} \rangle_\Omega := \frac{1}{V} \int_\Omega \boldsymbol{P} \ \mathrm{d}\Omega. \tag{31}$$

5.2 Boundary Conditions

Based on the construction of polycrystalline structures according to Sec. 4, polycrystals of several sizes are modelled, representing the microstructure of the polycrystalline material, see Fig. 2. For a RVE various boundary conditions are possible; uniform displacements can be applied leading to a stiffer response than the real response, uniform traction boundary conditions end in a softer response. Also periodic boundary conditions are possible, however, the VORONOI cell generation is complex for periodic structures. Further, a window of pre-homogenised material properties can be added to the boundary of the polycrystalline microstructure, the response in this case is yet scattering and presumes a larger computational expense. Within this contribution, uniform displacements are chosen which also enable the realisation of volumetric and deviatoric deformations. The displacement field $\boldsymbol{u}$ is given through a constant displacement gradient $\boldsymbol{H}$ on the entire boundary of the polycrystal

$$\boldsymbol{u}|_{\mathrm{d}\Omega} = \boldsymbol{H} \cdot \boldsymbol{X}|_{\mathrm{d}\Omega}\,, \quad \boldsymbol{H} = \text{const.} \tag{32}$$

Hence, the microscopic and macroscopic stress power are equal following the HILL theorem, and the eventually found RVE can be considered as statistically representative

$$\langle \boldsymbol{P} : \dot{\boldsymbol{F}} \rangle_\Omega = \langle \boldsymbol{P} \rangle_\Omega : \langle \dot{\boldsymbol{F}} \rangle_\Omega. \tag{33}$$

5.3 Overall Polycrystalline Behaviour

Differently sized polycrystals, from a size edge range between 100 and 200 μm, see Fig. 7, are subjected to pure shear loading through the displacement gradient $\boldsymbol{H} = \gamma\, \boldsymbol{e}_1 \otimes \boldsymbol{e}_2$. The number of crystal grains depend

on the size and are shown in Tab. 2. The material parameters for all the microstructures are equal; it is the bulk modulus $\kappa = 152.2$ GPa, the shear modulus $\mu = 79.3$ GPa, and the parameters for the viscoplastic range amount to $\tau_{y\,0} = 180$ MPa, $\dot{\gamma}_0 = 0.0005$, $H = 1.0$ GPa and $m = 3.0$. The chosen material parameters do not affect the qualitative behaviour of the microstructure and have to be determined later on for the overall material response in terms of parameters for an effective model. In order to obtain a statistically admissible response of the microstructure, 200 tests are computed for each size with body-centered cubic crystals with 24 slip system vectors of Tab. 1.

Table 1: 24 slip system vectors for body-centered cubic crystals

$\bar{\boldsymbol{s}}^\alpha$	$\bar{\boldsymbol{m}}^\alpha$	$\bar{\boldsymbol{s}}^\alpha$	$\bar{\boldsymbol{m}}^\alpha$	$\bar{\boldsymbol{s}}^\alpha$	$\bar{\boldsymbol{m}}^\alpha$	$\bar{\boldsymbol{s}}^\alpha$	$\bar{\boldsymbol{m}}^\alpha$	$\bar{\boldsymbol{s}}^\alpha$	$\bar{\boldsymbol{m}}^\alpha$	$\bar{\boldsymbol{s}}^\alpha$	$\bar{\boldsymbol{m}}^\alpha$
$[\bar{1}11]$	$(0\bar{1}1)$	$[\bar{1}11]$	(101)	$[\bar{1}11]$	(110)	$[\bar{1}11]$	(211)	$[\bar{1}11]$	$(12\bar{1})$	$[\bar{1}11]$	$(1\bar{1}2)$
$[111]$	$(0\bar{1}1)$	$[111]$	$(\bar{1}01)$	$[111]$	$(\bar{1}10)$	$[111]$	$(\bar{2}11)$	$[111]$	$(1\bar{2}1)$	$[111]$	$(11\bar{2})$
$[11\bar{1}]$	(011)	$[11\bar{1}]$	(101)	$[11\bar{1}]$	$(\bar{1}10)$	$[11\bar{1}]$	$(2\bar{1}1)$	$[11\bar{1}]$	$(\bar{1}21)$	$[11\bar{1}]$	(112)
$[1\bar{1}1]$	(011)	$[1\bar{1}1]$	$(\bar{1}01)$	$[1\bar{1}1]$	(110)	$[1\bar{1}1]$	$(21\bar{1})$	$[1\bar{1}1]$	(121)	$[1\bar{1}1]$	$(\bar{1}12)$

Table 2: Number of grains for polycrystal edge sizes

bounding box size edge [μm]	100	110	130	140	150	180	200
number of grains	6	13	20	32	45	107	157

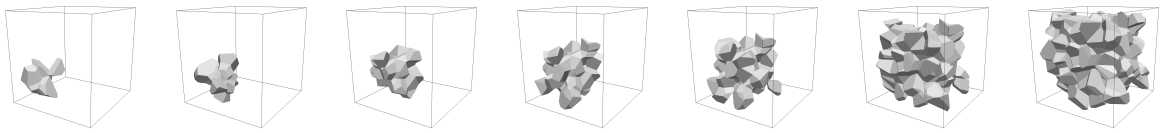

(a) 100 μm (b) 110 μm (c) 130 μm (d) 140 μm (e) 150 μm (f) 180 μm (g) 200 μm

Figure 7: Polycrystals of different sizes. The shown cube represents a bounding box of size $200 \times 200 \times 200$ μm.

As an example, the overall stress-strain relations for 200 polycrystalline structures of edge size 100 and 200 μm, respectively, are shown in Fig. 8. The response is quite stiff as expected. Given are the mean values of $[\langle \boldsymbol{P} \rangle_\Omega]_{12}$ over $[\langle \boldsymbol{F} \rangle_\Omega]_{12}$ of all computations with the variation of results in terms of ocurring minimal and maximal values. Whereas the response of the smaller polycrystal shows a rather scattering stress-strain behaviour due to the remaining high influence of the boundary loading, the larger polycrystal presents a more distinct behaviour of the microstructure. Expressing this in terms of the relative error in the homogenised 1st PIOLA-KIRCHHOFF stresses $\langle \boldsymbol{P} \rangle_\Omega$, the error $\frac{[\langle \boldsymbol{P} \rangle_\Omega]_{12}^{\mathrm{num},k} - \overline{[\langle \boldsymbol{P} \rangle_\Omega]}}{\overline{[\langle \boldsymbol{P} \rangle_\Omega]}}$ reaches the amount of $20\,\%$ and more over the whole deformation. Increasing the size of the polycrystal results in a decrease of the relative error to about $5\,\%$, which is the defined tolerance within this contribution.

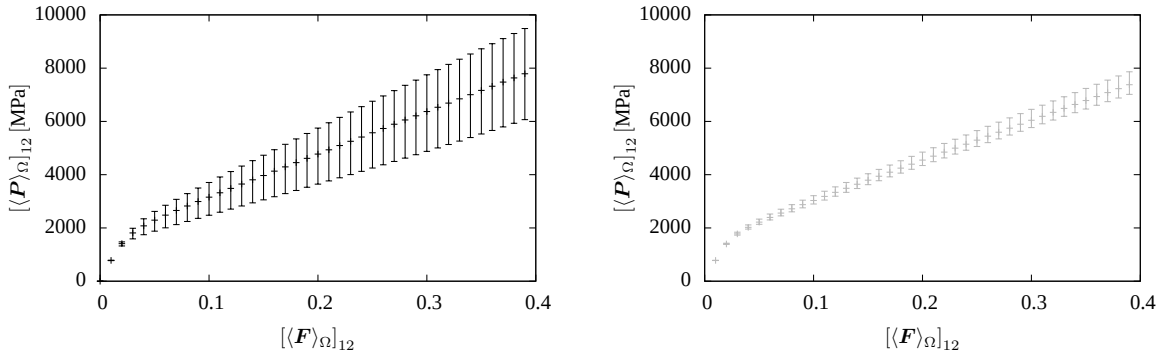

(a) Polycrystal within the bounding box $100 \times 100 \times 100$ μm. (b) Polycrystal within the bounding box $200 \times 200 \times 200$ μm.

Figure 8: Mean, minimal and maximal value of homogenised stress-strain responses of variously sized polycrystals.

The same effect applies for the normalised standard deviation $\sigma(\langle P_{ij}\rangle_\Omega)/\overline{||\langle P_{ij}\rangle_\Omega||}$ with

$$\sigma(\langle P_{ij}\rangle_\Omega) = \sqrt{\frac{1}{n}\sum_{k=1}^{n}\left(\langle P_{ij}\rangle_\Omega^k - \overline{\langle P_{ij}\rangle_\Omega}\right)^2} \tag{34}$$

$$\overline{\langle P_{ij}\rangle_\Omega} = \frac{1}{n}\sum_{k=1}^{n}\langle P_{ij}\rangle_\Omega^k \tag{35}$$

$$\overline{||\langle P_{ij}\rangle_\Omega||} = \frac{1}{n}\sum_{k=1}^{n}\left|\left|\langle P_{ij}\rangle_\Omega^k\right|\right| \tag{36}$$

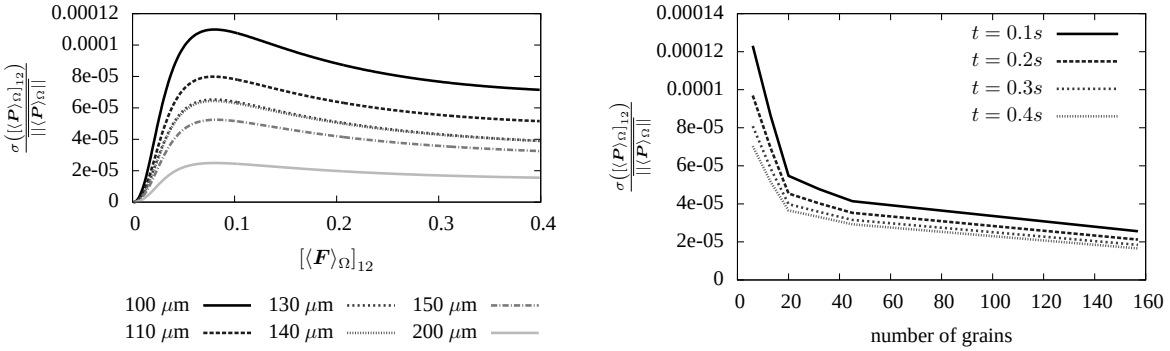

(a) Standard deviation over time.

(b) Standard deviation over grain number.

Figure 9: Normalised standard deviation of the polycrystals of different sizes for a population of 200 computations.

Fig. 9(a) shows the normalised standard deviation of the component $[\langle \boldsymbol{P}\rangle_\Omega]_{12}$ for different polycrystals over the deformation, Fig. 9(b) represents it over the polycrystal size in terms of the crystal grain quantity. From a grain number of about 20 on, the standard deviation does not decrease significantly anymore, whereas the $\pm\,5\,\%$ error measure requires polycrystalline structures of 100 grains and more.

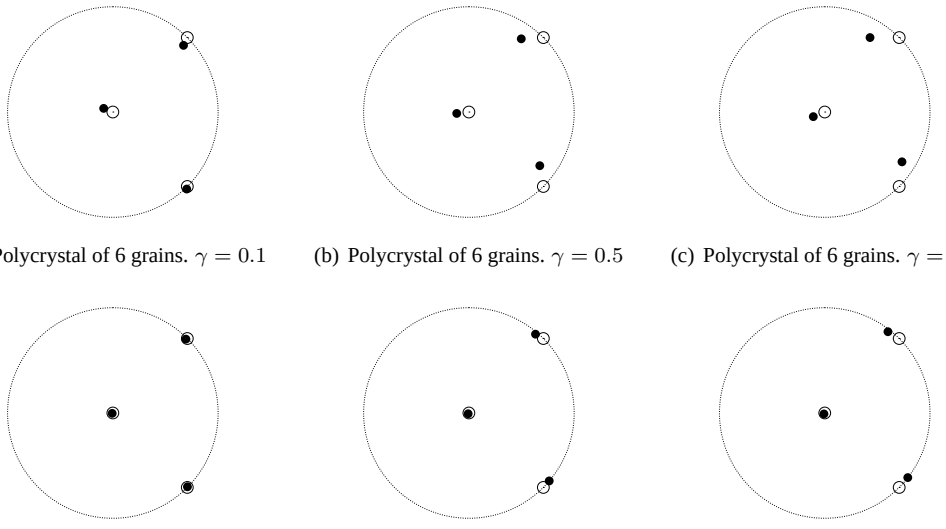

(a) Polycrystal of 6 grains. $\gamma = 0.1$ (b) Polycrystal of 6 grains. $\gamma = 0.5$ (c) Polycrystal of 6 grains. $\gamma = 0.7$

(d) Polycrystal of 157 grains. $\gamma = 0.1$ (e) Polycrystal of 157 grains. $\gamma = 0.5$ (f) Polycrystal of 157 grains. $\gamma = 0.7$

Figure 10: Stereographic projection of principal directions of homogenised 1st PIOLA-KIRCHHOFF $\langle \boldsymbol{P}\rangle_\Omega$ and deformation gradient $\langle \boldsymbol{F}\rangle_\Omega$ for pure shear $\langle \boldsymbol{F}\rangle_\Omega = \mathbf{1} + \gamma\, \boldsymbol{e}_1 \otimes \boldsymbol{e}_2$. Above a polycrystalline structure within $100 \times 100 \times 100$ μm (6 grains), below a polycrystalline structure within $200 \times 200 \times 200$ μm (157 grains).

The anisotropy which is induced by the plastic deformation is illustrated by the principal directions of a suitable stress and strain measure, $\langle \boldsymbol{P}\rangle_\Omega$ and $\langle \boldsymbol{F}\rangle_\Omega$ (Fig. 10). With the evolution of the plastic state, the principal axes rotate against each other and thus, stress and strain do not commute with each other once plastic deformation

occurs. The above figures, Figs. 10(a) to 10(c), show the stereographic projection of the principal directions for the small polycrystal of 6 grains; here, a more distinct rotation takes place than for the polycrystal of 157 grains in the lower figures (Figs. 10(d) to 10(f)). Due to the increasing boundary effect and the differently reoriented slip systems, the material behaves more isotropically and the direction of plastic deformation is not as perscribed as for fewer grains.

6 Conclusion and Outlook

6.1 Effective Material Properties

Assuming that the stresses from the volume averaging procedure are the same as from an effective material assumption

$$\langle \boldsymbol{P} \rangle_\Omega = \boldsymbol{P}^{\text{eff}} = \boldsymbol{P}(\langle \boldsymbol{F} \rangle_\Omega) = \boldsymbol{P}(\boldsymbol{F}^{\text{eff}}), \tag{37}$$

the determination of the effective material parameters can be performed based on a least square fit between the mean stresses out of n performed computations and the stresses from an effective constitutive assumption

$$\Pi := \left[\frac{1}{n} \sum_{k=1}^{n} \left(\langle \boldsymbol{P} \rangle_\Omega^k \right) - \boldsymbol{P}(\boldsymbol{F}^{\text{eff}}(\boldsymbol{\kappa}^{\text{eff}})) \right]^2 \rightarrow \text{minimum} \tag{38}$$

$$\boldsymbol{\kappa}^{\text{eff}} := \left[\boldsymbol{\kappa}_{el}^{\text{eff}}, \boldsymbol{\kappa}_{pl}^{\text{eff}} \right]^T. \tag{39}$$

Due to the volumetric-deviatoric split of the constitution, see (10), both parts of the deformation can be separated and reveals quite an easy way to determine first the isotropic elastic material parameters $\boldsymbol{\kappa}_{el}^{\text{eff}}$ by remaining in the elastic range of the deformation. Having determined the parameters with (38), also for varying elastic parameters within the crystal grains, the assignment of the plastic parameters $\boldsymbol{\kappa}_{pl}^{\text{eff}}$ can be done. Eventually, the gained effective material model representing the microstructural behaviour has to be validated for different kinds of boundary conditions and constraints of real forming processes.

7 Acknowledgements

Financial support for this research was provided by the Deutsche Forschungsgemeinschaft (DFG) under grant SFB TR 73.

References

Anand, L.: Single-crystal elasto-viscoplasticity: Application to texture evolution in polycrystalline metals at large strains. *Comput. Meth. Appl. Mech. Eng.*, 193, (2004), 5359–5383.

Anand, L.; Kothari, M.: A computational procedure for rate-independent crystal plasticity. *J. Mech. Phys. Solids*, 44, 4, (1996), 525–558.

Asaro, R. J.: Crystal plasticity. *J. Appl. Mech.*, 50, (1983), 921–934.

Brekelmans, W. A. M.: Crystal plasticity. In: *Constitutive Modeling of Solids – Mechanical Characterization*, chap. 8, Lecture Notes (course 4H100), Faculteit Werktuigbouwkunde, TU/e Eindhoven (2006).

Bridgman, P. W.: The thermodynamics of plastic deformation and generalized entropy. *Rev. Mod. Phys.*, 22, 1, (1950), 56–63.

de Souza, E. A.; Perić, D.; Owen, D. R. J.: *Computational Methods For Plasticity. Theory and Applications*. John Wiley and Sons Ltd Publication (2008).

de Souza Neto, E. A.: The exact derivative of the exponential of an unsymmetric tensor. *Comput. Meth. Appl. Mech. Eng.*, 190, (2001), 2377–2383.

Green, A. E.; Naghdi, P. M.: A general theory of an elastic-plastic continuum. *Arch. Ration. Mech. Anal.*, 18, (1965), 251–281.

Havner, K. S.: *Finite Plastic Deformation of Crystalline Solids*. Cambridge University Press (1992).

Lee, E. H.: Elastic-plastic deformation at finite strains. *J. Appl. Mech.*, 36, (1969), 1–6.

Mandel, J.: Plasticité classique et viscoplasticité. In: *CISM Courses and Lectures, no. 97*, Springer, Berlin (1972).

Miehe, C.: Exponential map algorithm for stress updates in anisotropic multiplicative elastoplasticity for single crystals. *Int. J. Numer. Methods Eng.*, 39, (1996), 3367–3390.

Miehe, C.; Schrder, J.; Schotte, J.: Computational homogenization analysis in finite plasticity: Simulation of texture development in polycrystalline materials. *Comput. Meth. Appl. Mech. Eng.*, 171, (1999), 387–418.

Needleman, A.; Asaro, R. J.; Lemonds, J.; Peirce, D.: Finite element analysis of crystalline solids. *Comput. Meth. Appl. Mech. Eng.*, 52, (1985), 689–708.

Schmid, E.; Boas, W.: *Plasticity of crystals with special reference to metals*. London Chapman & Hall Ltd (1968).

Steinmann, P.; Stein, E.: On the numerical treatment and analysis of finite deformation ductile single crystal plasticity. *Comput. Meth. Appl. Mech. Eng.*, 129, (1996), 235–254.

Address: Dipl.-Ing. Eva Lehmann and Dr.-Ing. Stefan Löhnert and Prof. Dr.-Ing. habil. Peter Wriggers, Leibniz Universität Hannover, Institut für Kontinuumsmechanik, 30167 Hannover, Germany.
email: lehmann@ikm.uni-hannover.de; loehnert@ikm.uni-hannover.de; wriggers@ikm.uni-hannover.de